

## Evidence of mini-jet emission in a large emission zone from a magnetically-dominated gamma-ray burst jet

S.-X. YI,<sup>1</sup> C.-W. WANG,<sup>1,2</sup> X. SHAO,<sup>3</sup> R. MORADI,<sup>1</sup> H. GAO,<sup>3</sup> B. ZHANG,<sup>4,5</sup> S.-L. XIONG,<sup>1</sup> S.-N. ZHANG,<sup>1,2</sup> W.-J. TAN,<sup>1,2</sup> J.-C. LIU,<sup>1,2</sup> W.-C. XUE,<sup>1,2</sup> Y.-Q. ZHANG,<sup>1,2</sup> C. ZHENG,<sup>1,2</sup> Y. WANG,<sup>6,7,8</sup> P. ZHANG,<sup>1,9</sup> Z.-H. AN,<sup>1</sup> C. CAI,<sup>10</sup> P.-Y. FENG,<sup>1,2</sup> K. GONG,<sup>1</sup> D.-Y. GUO,<sup>1</sup> Y. HUANG,<sup>1</sup> B. LI,<sup>1</sup> X.-B. LI,<sup>1</sup> X.-Q. LI,<sup>1</sup> X.-J. LIU,<sup>1</sup> Y.-Q. LIU,<sup>1</sup> X. MA,<sup>1</sup> W.-X. PENG,<sup>1</sup> R. QIAO,<sup>1</sup> L.-M. SONG,<sup>1</sup> J. WANG,<sup>1</sup> P. WANG,<sup>1</sup> Y. WANG,<sup>1,2</sup> X.-Y. WEN,<sup>1</sup> S. XIAO,<sup>11</sup> Y.-B. XU,<sup>1</sup> S. YANG,<sup>1</sup> Q.-B. YI,<sup>1,12</sup> D.-L. ZHANG,<sup>1</sup> F. ZHANG,<sup>1</sup> H.-M. ZHANG,<sup>1</sup> J.-P. ZHANG,<sup>1,2</sup> Z. ZHANG,<sup>1</sup> X.-Y. ZHAO,<sup>1</sup> Y. ZHAO,<sup>1,13</sup> AND S.-J. ZHENG<sup>1</sup>

<sup>1</sup>Key Laboratory of Particle Astrophysics, Institute of High Energy Physics, Chinese Academy of Sciences, Beijing 100049, China

<sup>2</sup>University of Chinese Academy of Sciences, Chinese Academy of Sciences, Beijing 100049, China

<sup>3</sup>Department of Astronomy, Beijing Normal University, Beijing 100875, People's Republic of China

<sup>4</sup>Nevada Center for Astrophysics, University of Nevada Las Vegas, NV 89154, USA

<sup>5</sup>Department of Physics and Astronomy, University of Nevada Las Vegas, NV 89154, USA

<sup>6</sup>ICRANet, Piazza della Repubblica 10, I-65122 Pescara, Italy

<sup>7</sup>ICRA, Dipartimento di Fisica, Sapienza Università di Roma, Piazzale Aldo Moro 5, I-00185 Rome, Italy

<sup>8</sup>INAF, Osservatorio Astronomico d'Abruzzo, Via M. Maggini snc, I-64100, Teramo, Italy

<sup>9</sup>College of Electronic and Information Engineering, Tongji University, Shanghai 201804, China

<sup>10</sup>College of Physics and Hebei Key Laboratory of Photophysics Research and Application, Hebei Normal University, Shijiazhuang, Hebei 050024, China

<sup>11</sup>Guizhou Provincial Key Laboratory of Radio Astronomy and Data Processing, Guizhou Normal University, Guiyang 550001, China

<sup>12</sup>School of Physics and Optoelectronics, Xiangtan University, Yuhu District, Xiangtan, Hunan, 411105, China

<sup>13</sup>School of Computer and Information, Dezhou University, Dezhou 253023, China

### ABSTRACT

The second brightest GRB in history, GRB230307A, provides an ideal laboratory to study the mechanism of GRB prompt emission thanks to its extraordinarily high photon statistics and its single episode activity. Here we demonstrate that the rapidly variable components of its prompt emission compose an overall broad single pulse-like profile. Although these individual rapid components are aligned in time across all energy bands, this overall profile conspires to show a well-defined energy-dependent behavior which is typically seen in single GRB pulses. Such a feature demonstrates that the prompt emission of this burst is from many individual emitting units that are casually linked in a emission site at a large distance from the central engine. Such a scenario is in natural consistency with the internal-collision-induced magnetic reconnection and turbulence framework, which invokes many mini-jets due to local magnetic reconnection that constantly appear and disappear in a global magnetically-dominated jet.

**Keywords:** Gamma-ray Bursts: Individual: GRB 230307A

sxyi@ihep.ac.cn

cwwang@ihep.ac.cn

gaohe@bnu.edu.cn

xiongs@ihep.ac.cn

### 1. INTRODUCTION

The origin of the prompt emission of gamma-ray bursts (GRBs) is still subject to debate because of the not-well-constrained jet composition, location of the emission region, and mechanism with which  $\gamma$ -rays are

produced (Zhang 2018). Depending on the unknown jet composition, three emission sites are commonly discussed in GRB prompt emission models. For a matter-dominated outflow, the observed emission is likely a superposition of a thermal component originating from the fireball photosphere at  $R_{\text{ph}} \sim 10^{11} - 10^{12}$  cm (Paczynski 1986; Goodman 1986; Mészáros & Rees 2000) and a non-thermal component originating from synchrotron-radiating electrons accelerated from internal shocks at  $R_{\text{IS}} \sim 10^{13} - 10^{14}$  cm (Rees & Meszaros 1994; Kobayashi et al. 1997; Daigne & Mochkovitch 1998a). There are also models with sub-photospheric dissipation (see Rees & Mészáros 2005a).

Alternatively, a GRB jet can be Poynting-flux-dominated which may dissipate its magnetic energy to power radiation. If dissipation occurs at small radii below the photosphere, the magnetic energy dissipation would mostly modify the spectrum of photospheric emission (Rees & Mészáros 2005b; Thompson et al. 2007; Giannios 2006; Drenkhahn & Spruit 2002). However, if the Poynting-flux energy is retained and gets dissipated only at a large-enough radius well above the photosphere, mini-jets can be generated through magnetic reconnection in a high- $\sigma$  ( $\sigma$  is defined as the ratio between Poynting flux and matter flux) flow with a typical mini-jet Lorentz factor  $\gamma \sim \sqrt{1 + \sigma}$ , and synchrotron radiation of the particles accelerated from these mini-jets will power fast-varying pulses in a GRB light curve (Lyutikov & Blandford 2003; Narayan & Kumar 2009; Zhang & Yan 2011). A well-developed model in this regime is the internal-collision-induced magnetic reconnection and turbulence (ICMART) model (Zhang & Yan 2011), which envisages an emission radius  $R_{\text{ICMART}} \sim 10^{15} - 10^{16}$  cm.

The extremely bright GRB 230307A was observed by Fermi (Fermi GBM Team 2023) and the Gravitational wave high-energy Electromagnetic Counterpart All-sky Monitor (GECAM) (Xiong et al. 2023) with trigger time of 15:44:06.650 UT on 7 March 2023. The Lobster Eye Imager for Astronomy (LEIA, the pathfinder of the Einstein Probe mission) also observed its prompt emission in the soft X-ray band (Sun et al. 2024). While the burst’s duration (measured as  $T_{90}$ ) of about 41 seconds aligns with the category of long-duration GRBs, the association of a kilonova (Levan et al. 2023a) and its unique properties in the prompt emission strongly suggest its origin from a compact binary merger event (Sun et al. 2024). As will be demonstrated in this article, intriguing features were discovered in the multi-band light curves of this burst. This provides us with unique evidence that the ICMART-like mechanism was at work in the prompt emission of GRB 230307A.

The paper is organized as follows: In the section **Observation**, we will describe the observation details of GRB 230307A; then in the following section **Analysis of the multi-band light curves**, we present the analysis of the multi-band data of the burst, and exhibit the aforementioned features; in the section **Physical implication**, we discuss in detail why these observational features can shed light on the prompt emission mechanism.

## 2. OBSERVATION

GRB 230307A triggered GECAM-B in real-time at 15:44:06.650 UT on 7 March 2023 (denoted as  $T_0$ ) and also detected by GECAM-C and other gamma-ray monitors (e.g. Fermi/GBM (Fermi GBM Team 2023), STIX (Xiao & Krucker 2023)), while GECAM-A was offline at that time<sup>1</sup>. The real-time alert data was transmitted instantly with the Global Short Message Communication of Beidou satellite navigation system (Zhao et al. 2021; Guo et al. 2023), and processed by the automatic pipeline of GECAM (Huang et al. (2023)), based on which the extreme brightness of GRB 230307A was reported by GECAM to the community (Xiong et al. 2023), initiating many multi-wavelength follow-up observations (Bom et al. 2023; Levan et al. 2023b). GRB 230307A is specially interesting because of its apparent single FRED shape in the overall light curve, and its high fluence and variability.

Thanks to the dedicated design of instrument (Zhang et al. 2023; Liu et al. 2021), neither GECAM-B nor GECAM-C suffered from data saturation during the whole burst of GRB 230307A despite of its extreme brightness (Sun et al. 2024). High quality of GECAM data allow us to accurately measure the temporal and spectral properties of GRB 230307A. GRD04 of GECAM-B and GRD01 of GECAM-C are selected for the analysis of light curves because of their smallest incident angle to the direction of GRB 230307A. These two

<sup>1</sup> GECAM is a dedicated all-sky gamma-ray monitor constellation funded by the Chinese Academy of Sciences, and now consists of three telescopes, i.e. GECAM-A and GECAM-B (Li et al. 2021) micro-satellites launched together on December 10, 2020, and GECAM-C (also called High Energy Burst Searcher, HEBS) (Zhang et al. 2023) onboard SATech-01 experimental satellite launched on July 27, 2022. There are two kinds of detectors in each GECAM telescope: Gamma-Ray Detectors (GRDs) and Charged Particle Detectors (CPDs). GRDs are the main detector of GECAM, each of which is composed of a scintillator and an array of SiPMs. There are 25 GRDs onboard each of GECAM-A and GECAM-B, and 12 GRDs onboard GECAM-C. GECAM is designed to have the highest time resolution (0.1  $\mu$ s) among all GRB detectors ever flown (Xiao et al. 2022), making it one of the most suitable detectors for conducting the temporal research about GRBs.

detectors both operate in two readout channels: high gain (HG) and low gain (LG), which are independent in terms of data processing, transmission, and dead-time. At the time of this burst, GECAM-C GRDs have a lower energy detection threshold of about 6 keV (owing to less radiation damage on SiPM) while GECAM-B GRDs have a relatively higher energy detection threshold of about 30 keV. For GRD04 of GECAM-B, the energy range of HG channel data are used from about 30 keV to 300 keV while the energy range of LG channel data are used from about 300 keV to 1000 keV. For GRD01 of GECAM-C, only HG channel data are used with the energy range from 6 keV to 30 keV. Though the response of GRD01 of GECAM-C for 6-15 keV and GRD04 of GECAM-B for 300-700 keV is affected by the electronics, this does not have any effect on the analysis of light curves. The background of GECAM-B is estimated by fitting the data from  $T_0-50$  s to  $T_0-5$  s and  $T_0+160$  s to  $T_0+200$  s with the first order polynomials. The background of GECAM-C is estimated by fitting the data from  $T_0-20$  s to  $T_0-1$  s and  $T_0+170$  s to  $T_0+600$  s with a combination of the first and second-order exponential polynomials (Sun et al. 2024). The observed light curves are not directly used to identify features of the broad pulse and fast pulses. Those features are identified through jointly fitting the background and the signals using various functional forms to describe pulses (see in the following section).

We have also cross-checked the GECAM data with that of Fermi/GBM, which has suffered from pile-up effects, which severely changed the shape of the light curve around the peak. For other part of the GBM data that did not suffer from pile-up, we performed the same analysis, including temporal analysis and spectral analysis. The results show well consistency with the GECAM results. We therefore do not include the GBM data in our following analysis.

### 3. ANALYSIS OF THE MULTIBAND LIGHT CURVES

#### 3.1. The Norris-like single pulse overall profile

The unsaturated data record by GECAM enable us to accurately characterize the temporal properties of GRB 230307A. The high time-resolution light curves show many rapidly varying structures in the prompt emission (see thin grey lines in Figure 1). Intriguingly, by comparing the light curves in different energy bands<sup>2</sup>, we found that the light curves also have slow varying

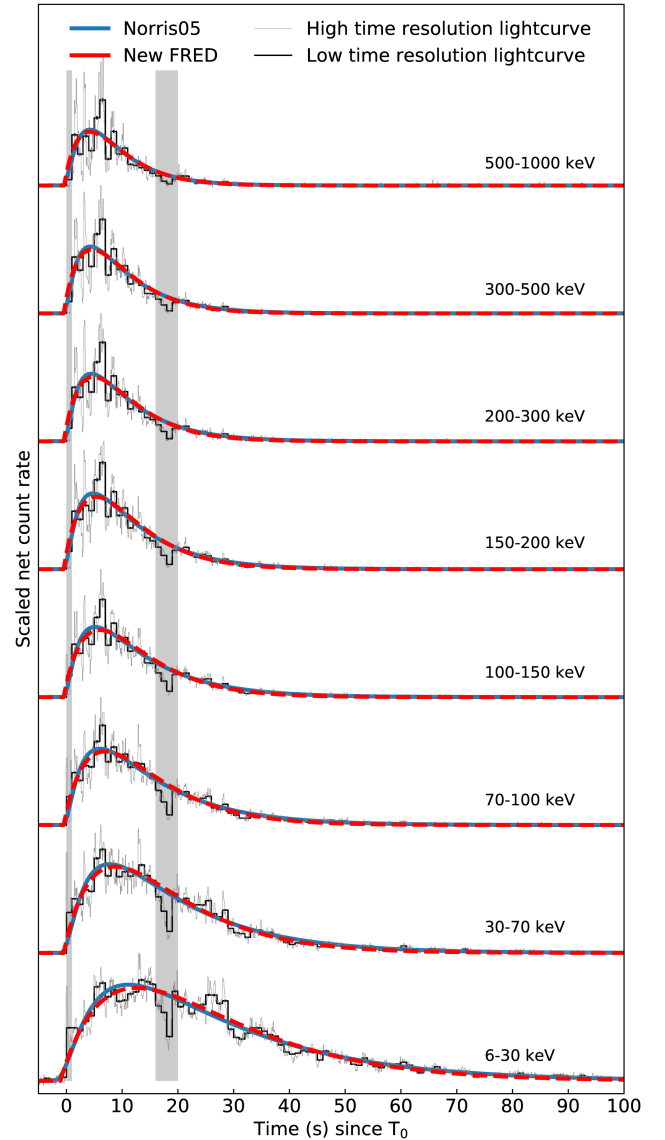


**Figure 1. The multi-band light curves.** The black histograms are 1 s binned net count rates (with background subtracted), whose profile shows a single FRED shape; The gray thin histograms are 0.1 s binned net count rates (with background subtracted); The blue solid curves are best-fit FRED model with the Norris05 formulation, while the blue dashed curves are the best-fit with our new FRED formulation. Gray shadowed regions (the precursor and the dip) are ignored in the fitting. All error bars represent  $1\sigma$  uncertainties of the net count rates.

trends, which are slower at lower energy bands (this can be better seen with lower time-resolution light curves. See the binned light curves in Figure 1). In order to quantitatively study the slow trends, we attempt to fit the low time-resolution light curves with a conventional parameterisation of the FRED (Fast Rise Exponential

<sup>2</sup> namely, 6-30 keV, where the data are from GECAM-C; 30-70 keV, 70-100 keV, 100-150 keV, 150-200 keV, 200-300 keV, 300-500 keV and 500-1000 keV, where the data are from GECAM-B

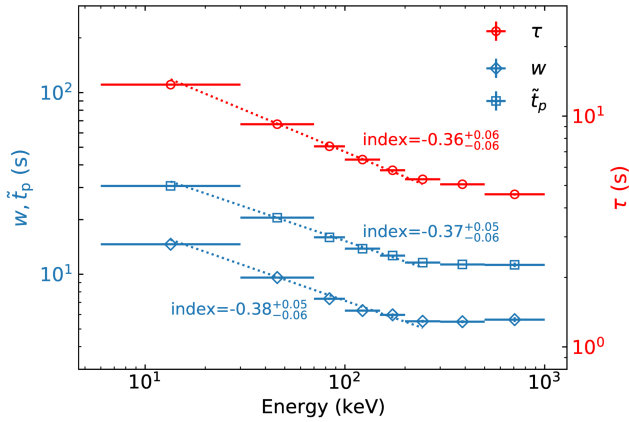


**Figure 2. The fitted FRED formulation parameters as a function of energy.** The vertical error bars indicate the  $1\sigma$  uncertainties of the fitted parameters, while the horizontal error bars indicate the ranges of the energy bins.

Decay) profile (Norris et al. 2005):

$$L(t) \propto \frac{1}{\exp\left(\frac{\tau_r}{t-t_s} + \frac{t-t_s}{\tau_d}\right)}. \quad (1)$$

In the above formulation,  $t_s$  is the starting instance of the profile,  $\tau_r$  and  $\tau_d$  are the rising and decaying time scales, respectively. In the fitting process, we assume that the net count (with background model subtracted) in each bin follows a Poisson probability distribution, with the expected value equal to the parameterized FRED profile. The fittings are done with the maximum likelihood method, which can be expressed as  $\ln\mathcal{L} = \sum_i [\text{MODEL}_i - \text{DATA}_i \ln(\text{MODEL}_i)]$ , where the subscript  $i$  runs over all time bins from -4s to 100s (excluding 0s to 1s and 16s to 20s) and the part used to estimate the background model. The posteriors of the fitted parameters are found with a Monte Carlo Markov Chain (MCMC) method.

The fitting results are listed in Table 1. The best-fit Norris FRED profiles are plotted with multi-band light curves in Figure 1. The peak time  $t_p$  and the width  $w$  of the are therefore defined as:  $t_p = t_s + \sqrt{\tau_r \tau_d}$  and  $w = \tau_r + \tau_d$ . It can be seen in Figure fig:1.5 that there is a clear energy dependence in both  $w$  and  $\tilde{t}_p \equiv t_p - t_s$ : In the energy range from 6 keV to 300 keV, the  $w - E$  and  $\tilde{t}_p - E$  relations are both in a power law function, with the power indices  $-0.38^{+0.05}_{-0.06}$  and  $-0.37^{+0.05}_{-0.06}$ , respectively. Above  $\sim 300$  keV, the energy dependence on both  $w$  and  $\tilde{t}_p$  saturate. Such a profile-energy dependence was commonly found in single GRB pulses (Norris et al. 2005; Liang et al. 2006; Hakkila et al. 2008; Peng et al. 2012).

### 3.2. The self-similarity of the overall profile

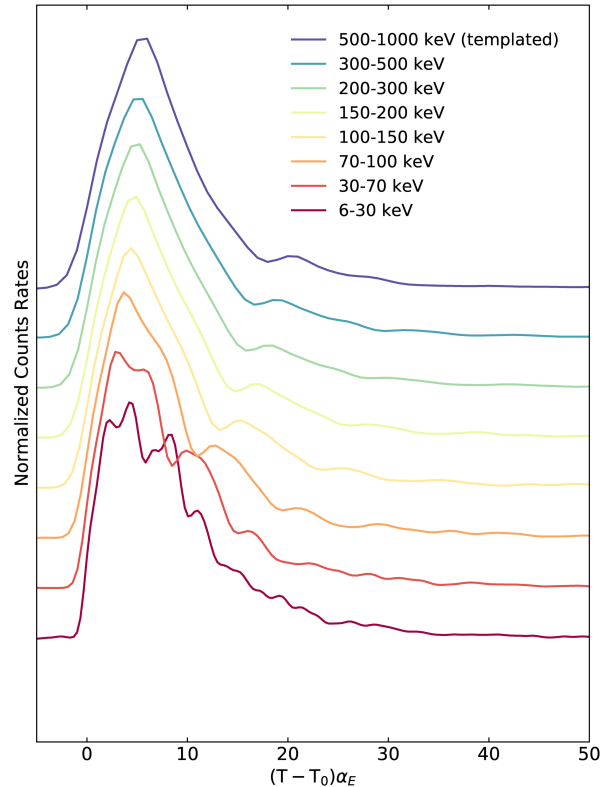


**Figure 3. The smoothed and time-rescaled GECAM multiband light curves of GRB 230307A**

We would like to further explore the profile-energy dependence. As we found above, the peak time and the width of the profile vary with energy with the same power law index. As a consequence, the overall profile of the light curve (the broad pulse) in each energy band is a time-stretch copy of that in the other bands (we follow the terminology of Ref. Norris et al. (2005) to call it a “self similar profile”). In order to further demonstrate the self-similar feature of the slow varying profile, we smooth the light curves in a non-parametrical way, and manifest their shape identity after energy-dependent re-scaling in time.

The smoothed light curves are convolution between a Gaussian kernel and the original light curves. The sigma of the Gaussian kernel is 1.5s. It can be obviously shown that, the shape of the profiles in different energy bands can be “stretched” in time domain into an identical shape with an energy dependent scaling factor. We use the smoothed light curve in the 500-1000 keV band as the template, and we fit the template to light curves in other bands, which are scaled by multiplying scaling factors  $\alpha_E$  to the their time argument  $T - T_0$ . We stack all the re-scaled and smoothed light curves in Figure 3. It is intuitively shown that the self-similarity of the broad profile, and this conclusion is FRED for-

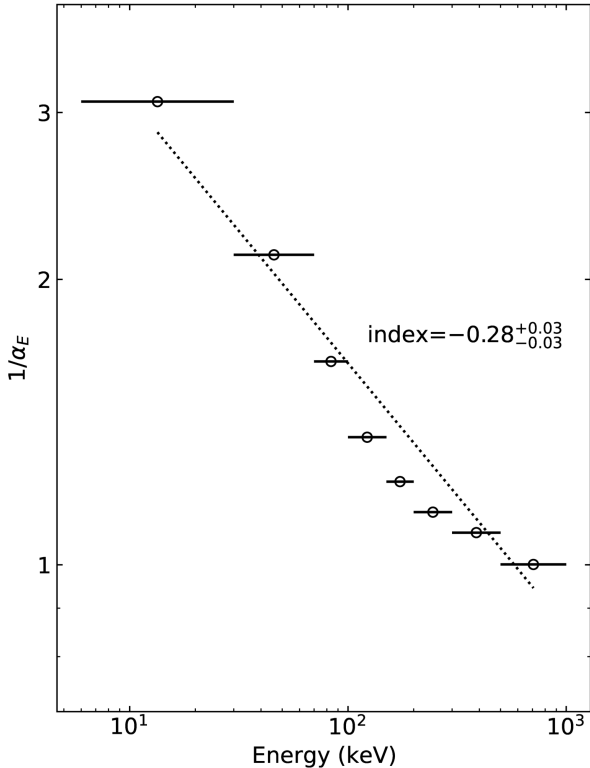


**Figure 4.** The scaling factor of the Gaussian smoothed light curve as a function of energy. The vertical error bars indicate the  $1\sigma$  uncertainties of the fitted parameters, while the horizontal error bars indicate the ranges of the energy bins.

mulation independent. The scaling factor as a function of energy is plotted in the Figure 4, which again shows a power law dependence.

The “self-similarity” inspired us to propose another formulation of FRED profile, with one less parameter than that of Norris05:

$$L(t) \propto \frac{t - t_s}{\tau} \exp\left(-\frac{t - t_s}{\tau}\right). \quad (2)$$

We fit the multi-band light curves again with the new FRED formulation. The results of fitting are listed in Table 1. The sole time scale parameter  $\tau$  shows a similar energy dependence on energy,  $\tau \propto E^{-0.36^{+0.06}_{-0.06}}$ , from 6 to 300 keV, and shows a hint of shallower energy dependence above  $\sim 300$  keV (Figure 2). In the new formulation, one can define peak time as  $t_p = t_s + \tau_E$ , where we denote the  $\tau$  in the  $E$  channel with  $\tau_E$ . The width of the FRED profile also scales as  $\tau_E$ . Therefore, the found  $\tau - E$  dependence can naturally result in the  $w - E$  and  $\tilde{t}_p - E$  relations.

### 3.3. The fast components

We subtract the slow trend described by equation 2 with the best-fit parameters, to study the fast varying

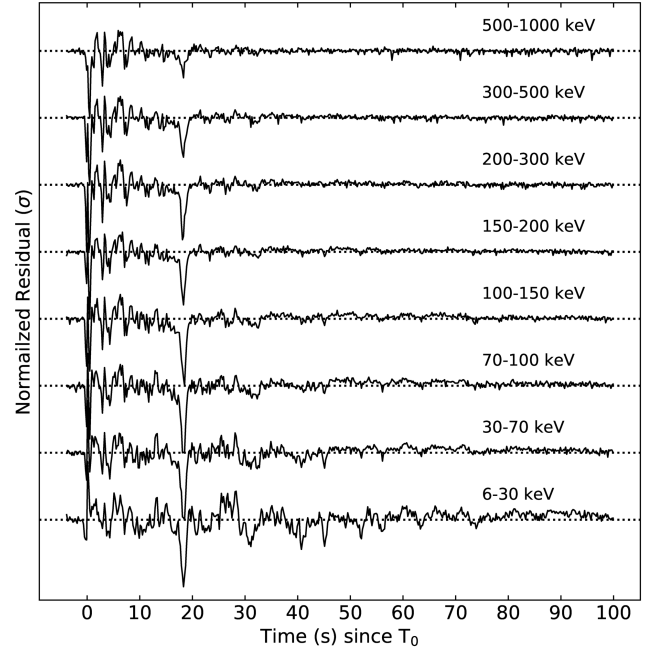


**Figure 5.** The residuals of the net light curves after fitting with the new FRED formulation

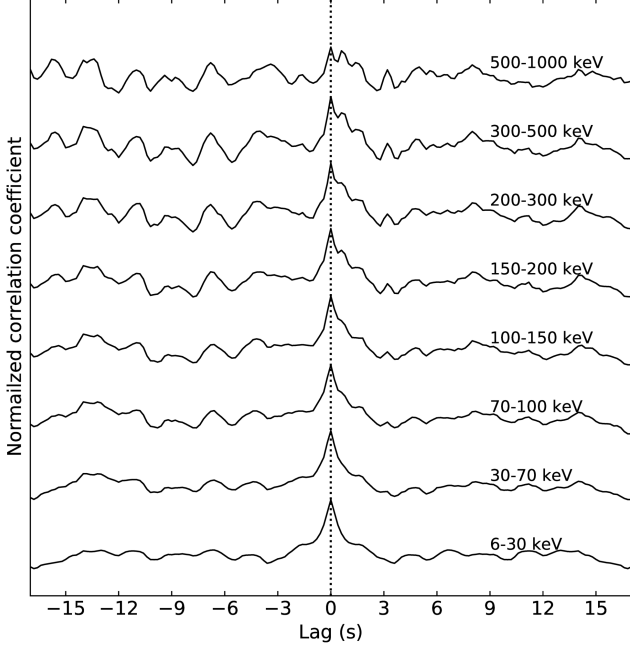
structures. From the residuals of the light curves (Figure 5), one can see that there are many rapidly-varying short pulses. One noticeable feature is that even the broad pulse has a clear energy dependence, the short time spikes and dips appear to align at the same instances across different energy bands.

We further demonstrate this alignment of the fast temporal features by cross-correlations among multi-band light curve residuals. As shown in the Figure 6, the peaks are perfectly aligned across the full energy band. This immediately excludes the attempt to explain the self-similar stretchable feature of the multi-band light curves as relativistic time-dilation, as a time-dilation effect would stretch both slow and fast varying pulses together.

Here we further demonstrate that some of the prominent fast structures can be identified as small pulses without an underlying slow component. For instance, we show that the spike at  $\sim 3.5$  s can be fitted with a pulse profile. We employ our new FRED formulation to fit the pulse from 3 s to 3.75 s, and find the typical width- $E$  relation ( $\tau - E$  in the new FRED formulation) in GRB pulses. In order to show this conclusion is independent on the pulse profile formulation, we use Gaussian function as an alternative profile to fit the spike, and obtain the same width- $E$  relation ( $\sigma - E$  with the Gaussian pulse formulation). See the lower panel of Figure 8. It can be seen in the Figure 7 that the FRED profile results in a better fit than the Gaussian profile. The fitted

**Table 1. Fitting results for the light curves of GRB 230307A.** All errors represent the  $1\sigma$  uncertainties.

Energy range (keV)	Norris05				New FRED		
	$\tau_r$ (s)	$\tau_d$ (s)	norm (counts·s <sup>-1</sup> )	$t_s$ (s)	$\tau$ (s)	norm (counts·s <sup>-1</sup> )	$t_s$ (s)
6-30	$10.78^{+0.31}_{-0.30}$	$19.87^{+0.13}_{-0.13}$	$2.49^{+0.06}_{-0.06} \times 10^4$	$-3.53^{+0.11}_{-0.11}$	$13.68^{+0.04}_{-0.04}$	$1.50^{+0.01}_{-0.01} \times 10^4$	$-1.08^{+0.04}_{-0.04}$
30-70	$6.65^{+0.20}_{-0.19}$	$13.85^{+0.10}_{-0.10}$	$2.04^{+0.05}_{-0.05} \times 10^4$	$-1.85^{+0.06}_{-0.06}$	$9.22^{+0.03}_{-0.03}$	$1.35^{+0.01}_{-0.01} \times 10^4$	$-5.00^{+0.08}_{-0.07} \times 10^{-1}$
70-100	$4.84^{+0.17}_{-0.17}$	$11.14^{+0.09}_{-0.09}$	$1.17^{+0.03}_{-0.03} \times 10^4$	$-1.31^{+0.06}_{-0.06}$	$7.40^{+0.03}_{-0.03}$	$8.20^{+0.05}_{-0.05} \times 10^3$	$-4.94^{+0.14}_{-0.07} \times 10^{-1}$
100-150	$4.09^{+0.13}_{-0.13}$	$9.74^{+0.07}_{-0.07}$	$1.44^{+0.04}_{-0.04} \times 10^4$	$-1.15^{+0.05}_{-0.05}$	$6.48^{+0.03}_{-0.03}$	$1.02^{+0.01}_{-0.01} \times 10^4$	$-4.96^{+0.09}_{-0.04} \times 10^{-1}$
150-200	$4.25^{+0.17}_{-0.17}$	$8.43^{+0.08}_{-0.08}$	$1.10^{+0.04}_{-0.04} \times 10^4$	$-1.19^{+0.06}_{-0.06}$	$5.82^{+0.03}_{-0.03}$	$6.88^{+0.05}_{-0.05} \times 10^3$	$-4.90^{+0.20}_{-0.10} \times 10^{-1}$
200-300	$4.00^{+0.18}_{-0.18}$	$7.59^{+0.08}_{-0.08}$	$1.07^{+0.04}_{-0.04} \times 10^4$	$-1.07^{+0.06}_{-0.06}$	$5.32^{+0.03}_{-0.03}$	$6.49^{+0.05}_{-0.05} \times 10^3$	$-4.83^{+0.28}_{-0.14} \times 10^{-1}$
300-500	$4.25^{+0.19}_{-0.18}$	$7.08^{+0.08}_{-0.08}$	$1.23^{+0.05}_{-0.05} \times 10^4$	$-1.20^{+0.06}_{-0.05}$	$5.06^{+0.03}_{-0.03}$	$6.77^{+0.05}_{-0.05} \times 10^3$	$-4.86^{+0.26}_{-0.13} \times 10^{-1}$
500-1000	$5.38^{+0.42}_{-0.39}$	$5.89^{+0.12}_{-0.12}$	$8.00^{+0.76}_{-0.67} \times 10^3$	$-1.41^{+0.10}_{-0.10}$	$4.58^{+0.05}_{-0.05}$	$3.09^{+0.04}_{-0.04} \times 10^3$	$-4.00^{+0.90}_{-0.71} \times 10^{-1}$

**Figure 6. The cross-correlation between the multi-band residuals and that in the 6-30 keV channel.** The vertical dotted line indicates the zero lag time.

parameters are list in Table 2. It is also interesting to observe that this small pulse does not show spectrum lag of its peak time as the broad pulse. We demonstrate this by cross-correlating between the small pulses in multi-bands and that in 30-70 keV channel. The lag time together with their uncertainties as a function of energy is shown in the upper panel of Figure 8, where all lag times are almost zero, and we can clearly conclude that the lag time does not depend on energy like the broad pulse.

### 3.4. The dip at around 18s

The dip at  $\sim 18$ s is another noticeable feature of the multi-band light curves. A natural attempt is to attribute such a dip to some sort of absorption or geometrical blocking. We define the effective “optical depth”

$\tau_{\text{op,E}}$  in different energy bands as:

$$\exp(-\tau_{\text{op,E}}) = \frac{C_{\text{dip,E}}}{C_{\text{slow,E}}}, \quad (3)$$

where  $C_{\text{dip}}$  is the net count rate at the bottom of the dip, which is found with a negative Gaussian fitting superposed on the FRED of broad pulse fitting from 17s to 19.5s (Figure 9); and  $C_{\text{slow}}$  is the net count rate of the broad feature. The results of the fitting with a negative Gaussian is tabulate in Table 3. It is intriguing to find that there is a power law energy dependence of the effective optical depth, and the best fit power law index is  $\sim 0.4$  (Figure 10). This energy dependence of the optical depth challenges the absorption picture, for there is no known absorption mechanism whose cross section proportional to energy to the order of  $\sim 0.4$  with a break at about 300keV. Beside, if we were to explain the dip as absorption, its depth and transience require that the absorbing object has a angular size comparable to that of the emission region, and a very high transverse angular velocity. That will either result in a superluminal transverse velocity of the blocking object, or highly coincidental absorption in our local.

A reasonable explanation of the dip is the gap between two successive fast temporal structures. In order to demonstrate, we fit a pulse profile (new FRED formulation) and a rising edge of another pulse (Norris05) to the dip at each energy bands from  $\sim 17$ s to 19.5s (Figure 11). The fitted parameters are list in Table 4. The time scale  $\tau$  of the earlier pulses as a function of energy is plotted in Figure 12, which shows clearly a typical power law energy dependence of pulse width.

### 3.5. Summary of the observation features

Here we summarize the intriguing features from observation: (a) the overall light curve resembles a classic “single pulse”, which is wider and peaks later in lower energies in a self-similar way; and (b) there is no underlying elementary single slow pulse and the apparent broad profile is composed with many fast pulses.

**Table 2. Light curves fitting results for the fast varying temporal structure of light curves at about 3.5 s . All errors represent the  $1\sigma$  uncertainties.**

Energy range (keV)	Gaussian			New FRED		
	$\mu$ (s)	$\sigma$ (s)	norm (counts·s <sup>-1</sup> )	$\tau$ (s)	norm (counts·s <sup>-1</sup> )	$t_s$ (s)
30-70	$3.36^{+0.01}_{-0.01}$	$3.23^{+0.16}_{-0.14} \times 10^{-1}$	$4.87^{+0.13}_{-0.13} \times 10^3$	$2.87^{+0.12}_{-0.11} \times 10^{-1}$	$1.38^{+0.04}_{-0.04} \times 10^4$	$2.99^{+0.01}_{-0.01}$
70-100	$3.38^{+0.01}_{-0.01}$	$2.72^{+0.12}_{-0.10} \times 10^{-1}$	$3.63^{+0.11}_{-0.11} \times 10^3$	$2.57^{+0.10}_{-0.09} \times 10^{-1}$	$1.02^{+0.03}_{-0.03} \times 10^4$	$3.02^{+0.004}_{-0.005}$
100-150	$3.39^{+0.01}_{-0.01}$	$2.57^{+0.08}_{-0.07} \times 10^{-1}$	$5.16^{+0.13}_{-0.13} \times 10^3$	$2.30^{+0.10}_{-0.09} \times 10^{-1}$	$1.47^{+0.04}_{-0.04} \times 10^4$	$3.07^{+0.01}_{-0.01}$
150-200	$3.40^{+0.01}_{-0.01}$	$2.09^{+0.06}_{-0.05} \times 10^{-1}$	$4.11^{+0.12}_{-0.12} \times 10^3$	$1.94^{+0.08}_{-0.07} \times 10^{-1}$	$1.15^{+0.04}_{-0.04} \times 10^4$	$3.11^{+0.005}_{-0.01}$
200-300	$3.38^{+0.01}_{-0.01}$	$2.01^{+0.05}_{-0.05} \times 10^{-1}$	$4.23^{+0.13}_{-0.12} \times 10^3$	$1.77^{+0.06}_{-0.06} \times 10^{-1}$	$1.22^{+0.04}_{-0.04} \times 10^4$	$3.11^{+0.005}_{-0.01}$
300-500	$3.39^{+0.005}_{-0.01}$	$2.00^{+0.05}_{-0.05} \times 10^{-1}$	$4.45^{+0.13}_{-0.13} \times 10^3$	$1.75^{+0.05}_{-0.05} \times 10^{-1}$	$1.30^{+0.04}_{-0.04} \times 10^4$	$3.12^{+0.003}_{-0.003}$
500-1000	$3.38^{+0.01}_{-0.01}$	$1.74^{+0.06}_{-0.05} \times 10^{-1}$	$2.25^{+0.10}_{-0.09} \times 10^3$	$1.49^{+0.06}_{-0.05} \times 10^{-1}$	$6.72^{+0.31}_{-0.29} \times 10^3$	$3.13^{+0.003}_{-0.003}$

**Table 3. Light curves fitting results for the dip and optical depth. All errors represent the  $1\sigma$  uncertainties.**

Energy range (keV)	$\mu$ (s)	$\sigma$ (s)	$C_{\text{slow},E}$ (counts·s <sup>-1</sup> )	Optical Depth
6-30	$18.26^{+0.01}_{-0.01}$	$4.76^{+0.14}_{-0.13} \times 10^{-1}$	$5.15^{+0.01}_{-0.01} \times 10^3$	$0.96^{+0.04}_{-0.03}$
30-70	$18.25^{+0.01}_{-0.01}$	$5.51^{+0.14}_{-0.14} \times 10^{-1}$	$3.67^{+0.01}_{-0.01} \times 10^3$	$1.56^{+0.06}_{-0.06}$
70-100	$18.21^{+0.02}_{-0.02}$	$6.10^{+0.19}_{-0.18} \times 10^{-1}$	$1.72^{+0.01}_{-0.01} \times 10^3$	$2.11^{+0.12}_{-0.11}$
100-150	$18.24^{+0.02}_{-0.02}$	$7.07^{+0.21}_{-0.21} \times 10^{-1}$	$1.73^{+0.01}_{-0.01} \times 10^3$	$2.22^{+0.12}_{-0.11}$
150-200	$18.20^{+0.02}_{-0.02}$	$6.76^{+0.26}_{-0.25} \times 10^{-1}$	$9.40^{+0.01}_{-0.01} \times 10^2$	$2.62^{+0.23}_{-0.20}$
200-300	$18.19^{+0.02}_{-0.02}$	$6.87^{+0.30}_{-0.28} \times 10^{-1}$	$7.20^{+0.01}_{-0.01} \times 10^2$	$3.14^{+0.49}_{-0.35}$
300-500	$18.19^{+0.03}_{-0.03}$	$7.29^{+0.35}_{-0.33} \times 10^{-1}$	$6.58^{+0.01}_{-0.01} \times 10^2$	$2.70^{+0.34}_{-0.27}$
500-1000	$18.09^{+0.06}_{-0.06}$	$8.36^{+0.82}_{-0.74} \times 10^{-1}$	$2.26^{+0.01}_{-0.01} \times 10^2$	$2.46^{+0.59}_{-0.39}$

**Table 4. Light curves fitting results for the gap with two successive fast temporal structures. All errors represent the  $1\sigma$  uncertainties.**

Energy range (keV)	pulse before gap			pulse after gap			additional constant (counts·s <sup>-1</sup> )
	$t_s$ (s)	$\tau$ (s)	norm (counts·s <sup>-1</sup> )	$t_s$ (s)	$\tau_r$ (s)	norm (counts·s <sup>-1</sup> )	
6-30	$16.70^{+0.09}_{-0.09}$	$4.25^{+0.50}_{-0.61} \times 10^{-1}$	$1.08^{+0.10}_{-0.09} \times 10^4$	$18.09^{+0.09}_{-0.15}$	$1.40^{+0.47}_{-0.26}$	$1.28^{+0.37}_{-0.18} \times 10^4$	$1.10^{+0.36}_{-0.37} \times 10^3$
30-70	$16.87^{+0.04}_{-0.04}$	$3.49^{+0.32}_{-0.33} \times 10^{-1}$	$7.80^{+0.45}_{-0.48} \times 10^3$	$18.16^{+0.08}_{-0.14}$	$1.26^{+0.42}_{-0.19}$	$9.04^{+2.34}_{-1.10} \times 10^3$	$2.79^{+1.83}_{-1.78} \times 10^2$
70-100	$16.93^{+0.03}_{-0.03}$	$2.98^{+0.23}_{-0.24} \times 10^{-1}$	$3.50^{+0.18}_{-0.18} \times 10^3$	$18.12^{+0.10}_{-0.17}$	$1.40^{+0.61}_{-0.30}$	$4.44^{+1.67}_{-0.75} \times 10^3$	$55.83^{+58.62}_{-39.54}$
100-150	$17.01^{+0.03}_{-0.05}$	$2.77^{+0.26}_{-0.26} \times 10^{-1}$	$3.21^{+0.18}_{-0.18} \times 10^3$	$18.20^{+0.08}_{-0.13}$	$1.37^{+0.52}_{-0.26}$	$3.89^{+1.35}_{-0.63} \times 10^3$	$56.33^{+49.89}_{-38.18}$
150-200	$16.92^{+0.03}_{-0.05}$	$2.65^{+0.24}_{-0.20} \times 10^{-1}$	$1.99^{+0.13}_{-0.13} \times 10^3$	$17.81^{+0.26}_{-0.56}$	$2.75^{+3.33}_{-1.15}$	$3.90^{+8.08}_{-1.68} \times 10^3$	$15.11^{+20.23}_{-10.95}$
200-300	$16.96^{+0.02}_{-0.04}$	$2.33^{+0.19}_{-0.17} \times 10^{-1}$	$1.62^{+0.13}_{-0.13} \times 10^3$	$16.74^{+0.71}_{-0.52}$	$11.02^{+6.15}_{-5.87}$	$3.15^{+8.85}_{-2.44} \times 10^4$	$9.67^{+13.79}_{-7.04}$
300-500	$17.00^{+0.02}_{-0.02}$	$2.09^{+0.19}_{-0.18} \times 10^{-1}$	$1.52^{+0.14}_{-0.13} \times 10^3$	$16.45^{+0.77}_{-0.34}$	$14.29^{+4.90}_{-7.65}$	$5.12^{+11.94}_{-4.30} \times 10^4$	$21.78^{+21.31}_{-14.96}$
500-1000	$16.99^{+0.04}_{-0.15}$	$2.15^{+0.64}_{-0.47} \times 10^{-1}$	$3.63^{+0.73}_{-0.76} \times 10^2$	$16.45^{+0.66}_{-0.34}$	$15.75^{+8.09}_{-7.46}$	$2.28^{+21.32}_{-1.99} \times 10^4$	$19.69^{+13.15}_{-12.91}$

In order to better demonstrate that the observed profile-energy dependence cannot be attributed to an underlying broad pulse, we perform the following analysis: we downscale the best-fit FRED-profiles in each energy bands, so that there are no negative residuals in the high time-resolution light curves. The rescaled broad FRED are the maximum allowed underlying broad pulses in each energy bands, we plot it in the Figure 13. The found rescaling factor is the fraction of fluence attributed from this broad pulse. We can see that the rescaling factor in most energy bands are found to be negligible, suggesting that the broad pulse-energy dependence cannot be attributed to an underlying broad pulse.

In other words, *the individual pulses “know” about each other.*

## 4. PHYSICAL IMPLICATIONS

The above features found in this burst indicate that individual fast pulses are correlated in time and energy. The implication of that is, the emission sites of individual pulses should be connected casually. It provides significant insights into the prompt emission mechanism and the composition of the jet.

### 4.1. The ICMART model

In the ICMART model (Zhang & Yan 2011; Zhang & Zhang 2014; Shao & Gao 2022), individual fast pulses are emitted from mini-jets launched by local magnetic reconnections. While all mini-jets are in the same expanding magnetically-dominated fluid (see illustration in Figure 14). The rise and fall of the FRED-like profile is mostly dictated by the rate of growth of the num-

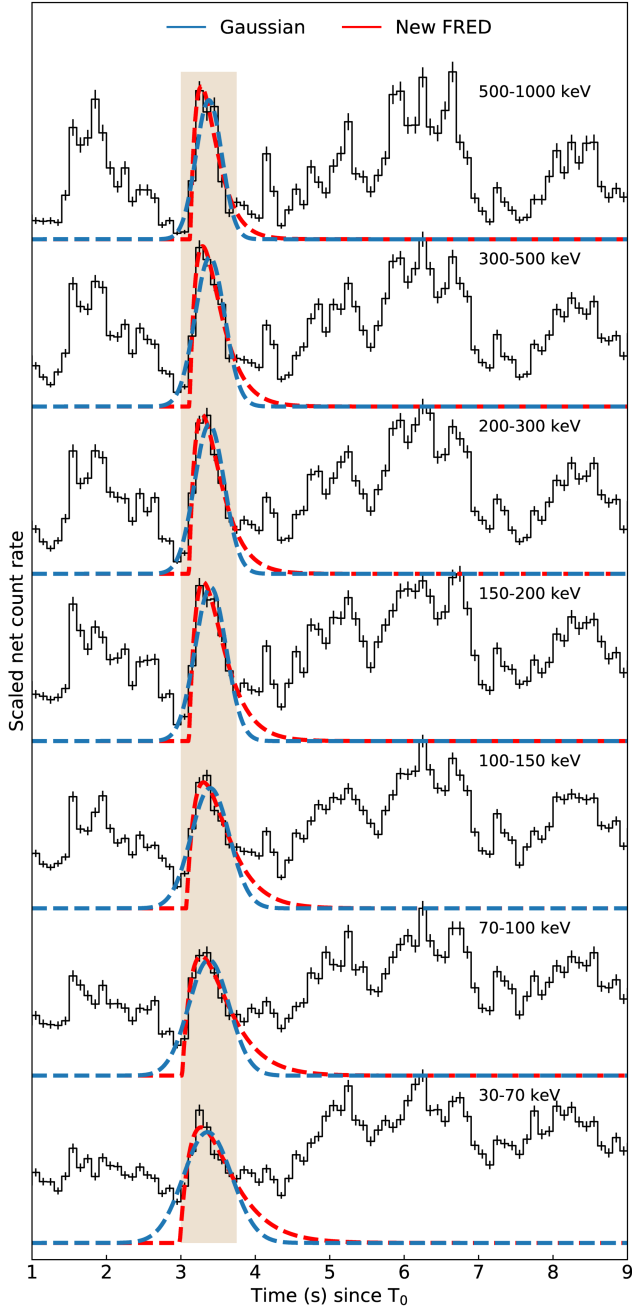


**Figure 7. Pulse profile fitting to the fast varying temporal structure at  $\sim 3.5$  s.** Red and blue dashed lines correspond to new FRED formulation and Gaussian profile respectively. The shadowed region indicates the range of data involved in the fitting.

ber of reconnection events (Yi et al. 2024). During the evolution of the broad pulse, the magnetic field strength decays as the whole fluid expands (Uhm & Zhang 2014). It leads to rolling down of the characteristic synchrotron emission frequency with time (Uhm & Zhang 2016; Uhm et al. 2018). The soften of the spectra over time leads to

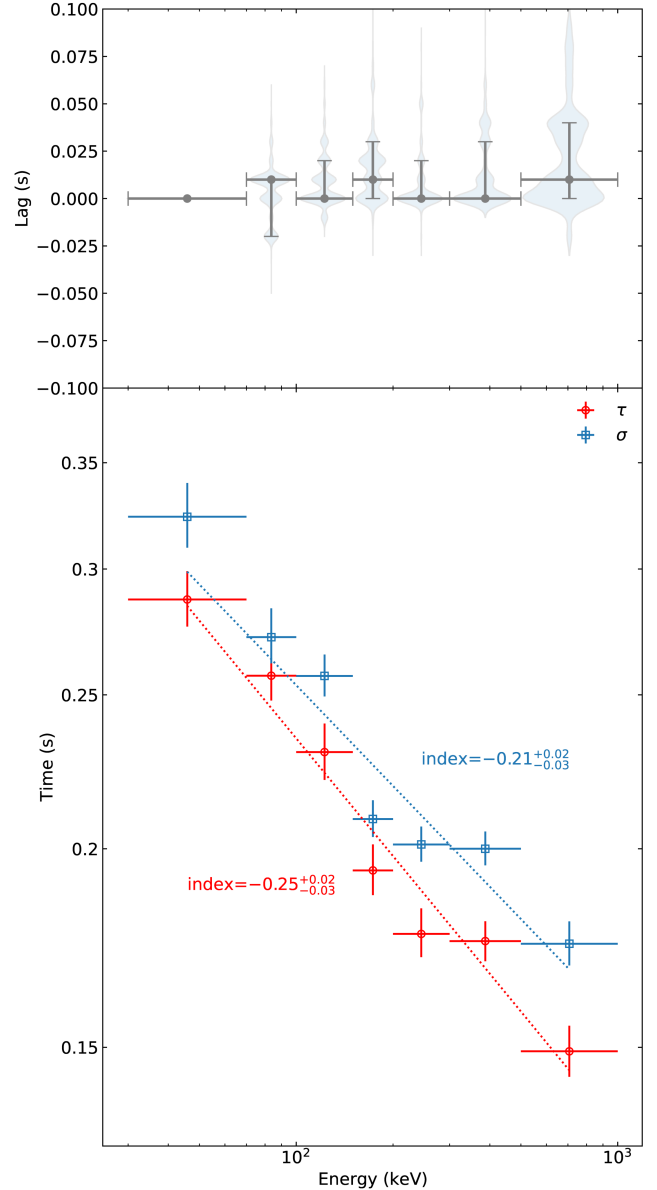


**Figure 8. Upper panel:** Cross-correlation between the light curves of small pulse in multi-bands as functions of the energy. **Lower panel:** The fitted width ( $\tau$  for new FRED and  $\sigma$  for Gaussian profile) of pulse at  $\sim 3.5$  s as function of energy.

the observed profile-energy dependence<sup>3</sup>. With certain spectrum evolution, a self-similar profile may be reproduced (Yi et al. 2024). Within this picture, the observed prompt emission originates from a single episode of central engine activity, which is consistent with the merger

<sup>3</sup> See Sun et al. (2024) for the spectrum time evolution analysis of this burst.



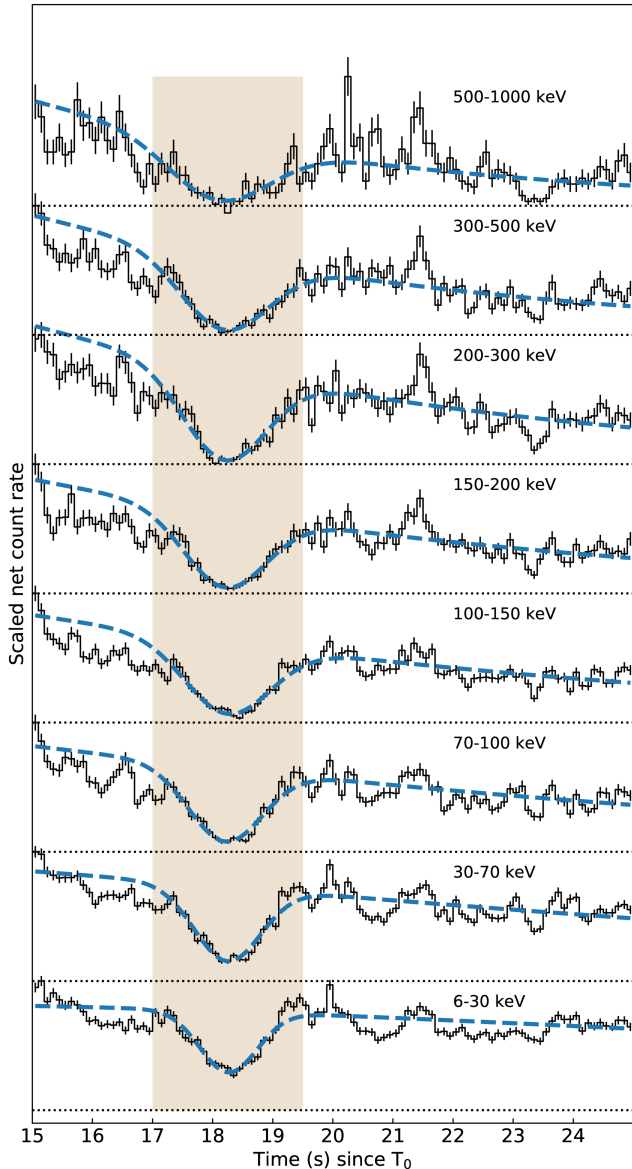


**Figure 9.** Fitting the gap with a FRED profile and a negative Gaussian function. The shadowed region indicates the range of data involved in the fitting

origin of GRB 230307A (Gillanders et al. 2023; Sun et al. 2024; Yang et al. 2024).

In order to better illustrate the idea, we conduct ICMART simulations and present the results. The general settings of the simulation are as follows: We assume a pair of magnetized shells collide and merge as one fluid after a collision at  $\sim 10^{15}$  cm. The mass of the fluid is assumed to be  $10^{31}$  g, the initial Lorentz factor is 30 the initial magnetization factor is  $\sigma = 50$  (i.e. the comoving-frame magnetic energy is 50 times of the rest-mass energy of the fluid). The number of reconnection events increases by a factor of 5 during the emission period and

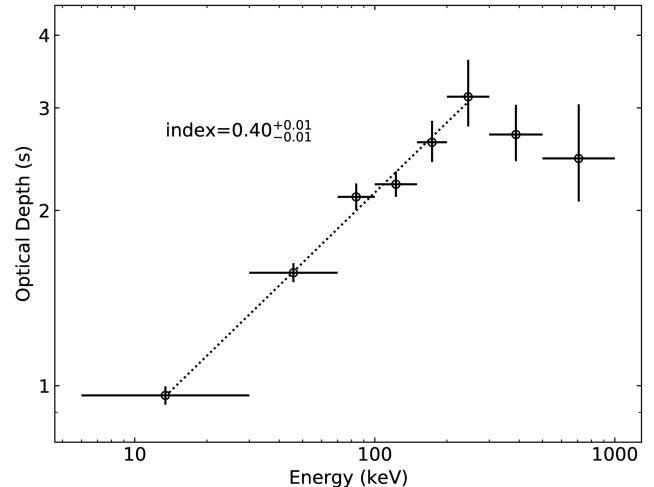


**Figure 10.** The effective optical depth defined with equation 3, as a function of energy.

the total number of the reconnection events within the  $1/\Gamma$  cone is assumed to be 200. The relatively small number of reconnection events was chosen to ensure the occurrences of dips in most of the realizations. Each reconnection event has a size of  $\sim 4 \times 10^{13}$  cm, a random latitude within  $(0, 1/3)$  and a random orientation within  $(0, \pi/2)$ . For each reconnection, the electrons are assumed to be accelerated to power law distribution with index  $-2.8$ . The electrons cool down and radiate via synchrotron radiation. We calculate the cooling and radiation process according to Uhm & Zhang (2014), and superpose the resulting synchrotron spectrum of each mini-jet to obtain the observed spectrum. In Figure 15, we show the light curves reproduced by the simulation that is consistent with the key observation features: 1) the light curve can be decomposed of many short pulses related to mini-jet emission; 2) the overall shape of the light curve resembles a single pulse, but can possess a very deep dip; 3) the overall single slow pulse has a significant shape evolution across energy bands. This simulation demonstrates that the ICMART model can well reproduce the observed behaviour of GRB 230307A. Detailed simulations will be presented in a separate paper.

#### 4.2. Standard internal shock model

The standard internal shock model, on the other hand, attributes short-time pulses as a consequence of collisions of many pairs of shells (see Figure 16 for an illustration). Within such a scenario, the overall trend is determined by the history of the central engine activity. Light curves in different bands should share this same history and should not display a global energy-dependent behaviour as observed.

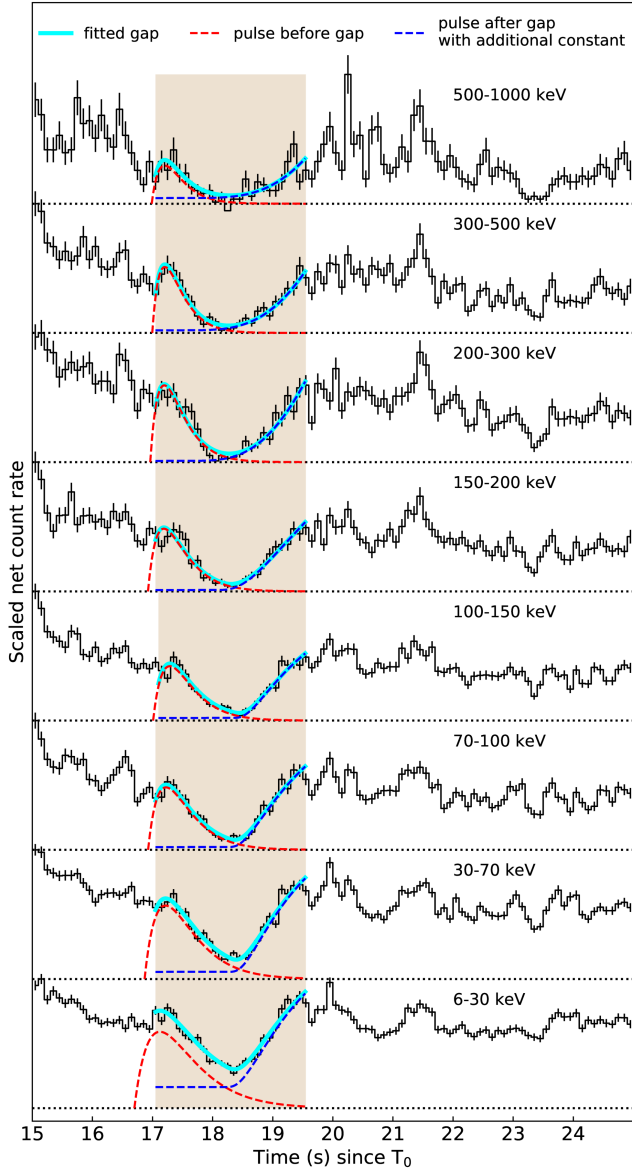


**Figure 11.** Fitting the gap with two successive short pulses. The dashed red curves indicate the earlier pulse component, and the dashed blue curves indicate the rising edge of the later pulse. Cyan curves indicating the summation of these two components.

To better demonstrate this, we conducted simulations within the framework of the standard IS model with the following settings: We simulated the ejection of 50 shells from the central engine, with their initial thicknesses, Lorentz factors and masses sampled from random distributions in the logarithmic space. The Lorentz factors vary from 100 to 1000, the mass ranges from  $10^{28}$  to  $10^{29}$ , and the initial thickness ranges from  $10^{10}$  to  $2 \times 10^{10}$ , all in cgs units. The central engine’s ejection times are randomly selected from a linear distribution,

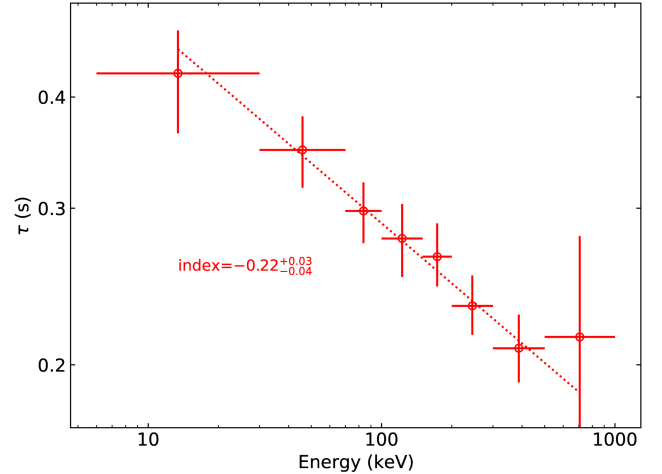


**Figure 12.** The time scale factor  $\tau$  for new FRED of the earlier pulse component in the 18-s dip, as a function of energy

with values ranging from 0 to 20 seconds in the rest frame of the GRB central engine. Upon each collision, two shells merge, and the merged shell parameters ( $m$ ,  $\gamma$ ,  $l_r$ ) are adopted as the new values for the remaining shell. To ensure tracking future collisions, the “effective” ejection time of this new shell is redefined as  $t_{ej,m} = R/c\beta_m$ , where  $\beta_m = (1 - 1/\gamma_m^2)^{1/2}$  and  $\gamma_m$  is the Lorentz factor of the merged shell. The simulation then restarts with one less shell. This process is repeated for each collision, allowing the code to monitor all collision/merging events for any arbitrarily designed central engine activity (Kobayashi et al. 1997; Maxham & Zhang 2009). The spectra for each pulse are simulated empirically (see details in a separate paper (Moradi et al. 2024)). The results of the simulation is presented in Figure 17, where there is no shape-energy dependence of the overall light curve as we expected. In the IS model, the energy-dependent lag and width generally apply to each pulse. Even if there is a stretching factor in low energies to make pulses broader, the stretching factor scales with the duration of short pulses. There is no way to reproduce a large stretching factor in the scale of the overall profile by superposing these short pulses.

#### 4.3. Modified internal shock model with another internal shock at large radius

A modified internal shock model (see Figure 18) may invoke another internal shock at a much larger emission radius (Daigne & Mochkovitch 1998b, 2003; Bošnjak & Daigne 2014) defined by  $R_2 \sim \Gamma^2 c \Delta t \sim (1.2 \times 10^{16} \text{ cm})(\Gamma/100)^2 (\Delta t/40 \text{ s})$ , where  $\Delta t \sim 40 \text{ s}$  is the timescale of the broad pulse. However, within such a picture, the observed emission should be the superposi-

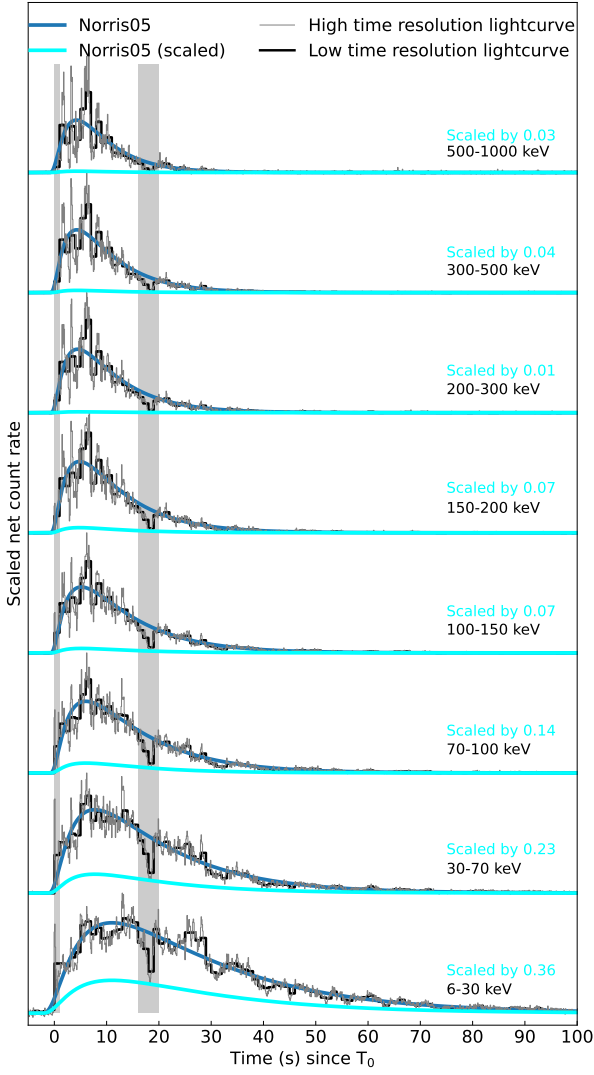


**Figure 13.** Maximum allowed underlying elementary broad pulses in each energy bands

tion between the fast and slow components, which requires that fast pulses only grow on top of a dominating the slow component. It is not supported by the existence of the very deep, achromatic dip at around 18 s.

We also conduct a simulation under this variant IS model: a separate shock at a larger distance ( $\sim 4 \times 10^{16}$  cm) is generated to make a slow pulse component that overlaps with those fast pulses. We consider synchrotron radiation process in IS model to determine the spectrum evolution of the long pulse, using the analytical solution proposed by [Daigne & Mochkovitch \(2003\)](#), involving a relativistic wind where a slower shell ( $\Gamma = 100$ ) decelerates a faster portion of the flow ( $\Gamma_0 = 400$ ) characterized by a constant rest-frame mass flux. The overall light curve is dominated by the slow pulse and

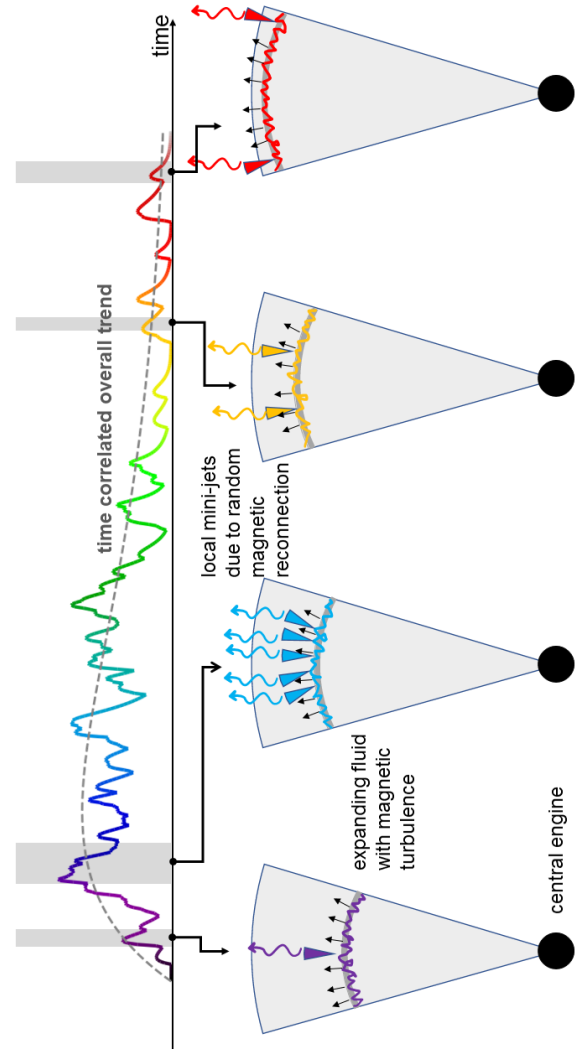


**Figure 14.** An illustration of the ICMART model.

The overall trend of the light curve corresponds to the growth and decline of the number of magnetic reconnection events within a single magnetized fluid. The turbulence in the fluid triggers random local reconnection events which emits through mini-jets. Each mini-jet emission corresponds to a fast pulse observed in the light curve. Because the emission originates from a single fluid that travels in space, a global shape-energy dependence is naturally expected. Deep dips are allowed in occasions when no bright mini-jets beam towards Earth at a particular epoch.

shows the shape-energy dependence (as illustrated in Figure 18). However, in this case, there should be a dominating underlying slow pulse emission component, which is in direct contradiction with the observations presented in this work. The corresponding simulation results are presented in Figure 19, which does not reproduce the observations, especially the deep dip.

In summary, any other attempt trying to model the prompt emission of this bursts within such frameworks

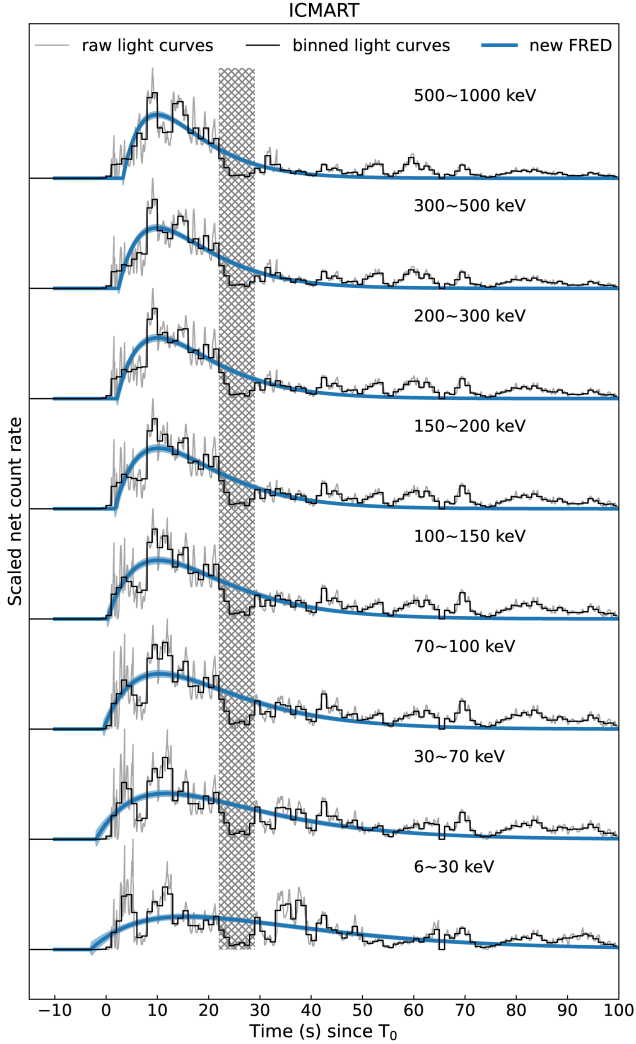


**Figure 15.** The simulated multi-band light curves within the framework of ICMART model. Both aligned short pulses and a global shape-energy dependence can be reproduced. The shaded area indicates the location of a reproduced light curve dip due to the lack of mini-jet emission at that time.

should manage to address all the aforementioned challenges.

## 5. SUMMARY

In this paper, we demonstrate that the light curve of GRB 230307A can be decomposed into several individual pulses, while the overall behavior of these individual pulses (slow varying trend) resembles a self-similar broad single pulse. While the rapid variability shows alignment in all energy bands, the broad pulse has a well-defined energy-dependence manner. In order to reach the above observational conclusion solidly, we conduct the following analysis:

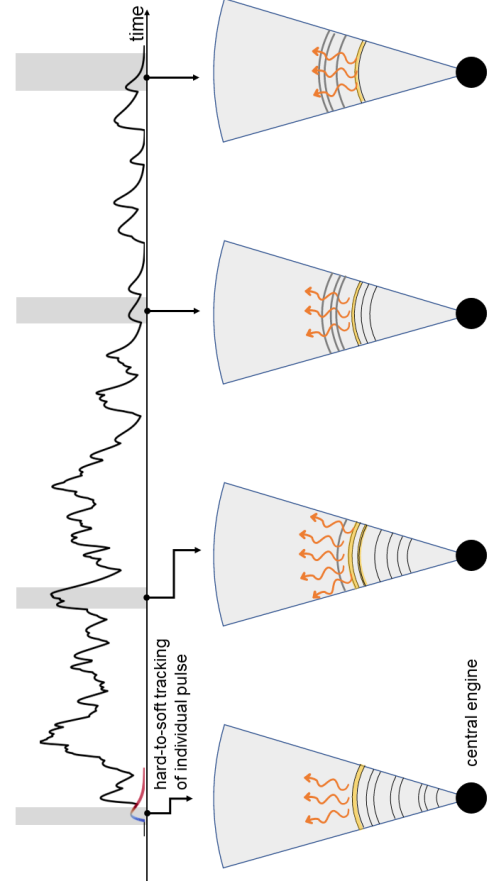


**Figure 16.** An illustration of the standard internal shock picture. Lower panels arranged from left to right depict the progression from earlier to later epochs. Each shock between a pair of shells (highlighted in lower panels) corresponds to a fast pulse in the light curve in the above panel (in corresponding shade regions). All collisions happen at similar distances from the central engine. Individual pulses may exhibit a spectral trend from hard to soft (illustrated with colour gradient). However, the overall light curve will not display any shape-energy dependence.

- We fit parameterized FRED profiles to the overall light curves in different energy bands, and found that the width and peak time of the profile decrease with the energy in a power law. This dependence was found to saturate at  $\sim 200$  keV;
- We found that the smoothed overall shape of the light curve in each band is essentially a time-stretched copy of that in the other bands;
- After subtraction of the overall trend of the light curve, we show that the residual variations superimposed on the best-fit "self-similar" temporal profile do not undergo the same temporal stretch-

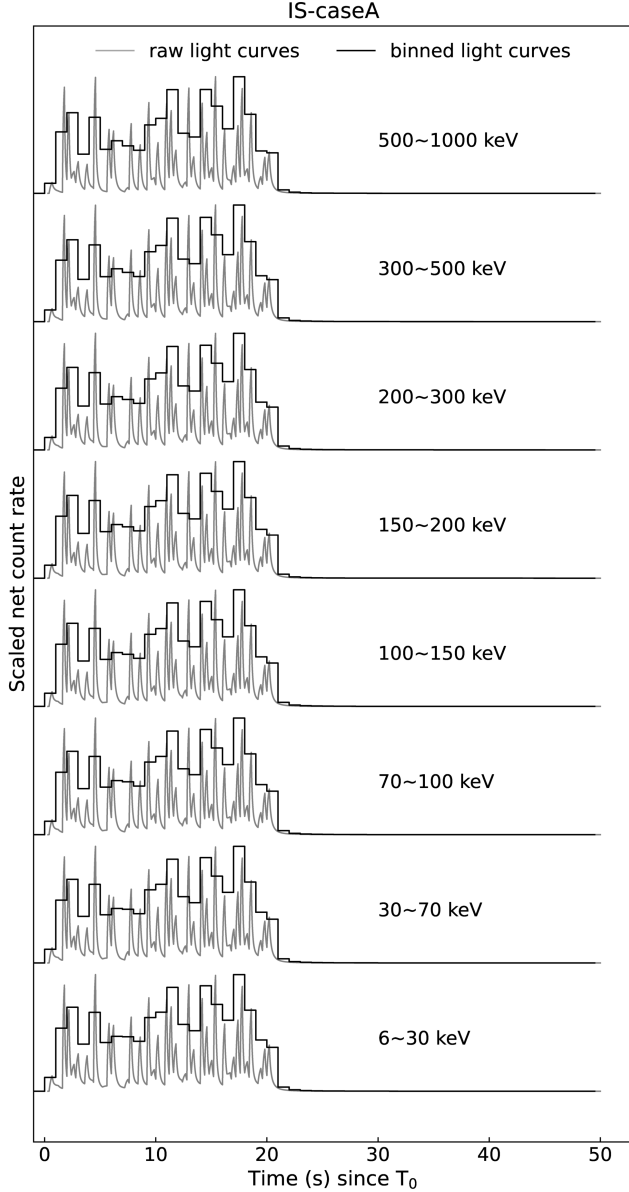


**Figure 17.** The simulated multi-band light curves within the framework of the standard internal shock model. It shows a random behaviour and the lack of global shape-energy dependence.

ing, but are instead fixed in time regardless of the band.

- We found that some prominent fast components can be fitted with individual pulses, such as the pulse at around 3.5s, and the dip at around 18s, without the need of an underlying slow components;
- The deep dip at around 18s significantly constrained any possible elementary slow components,

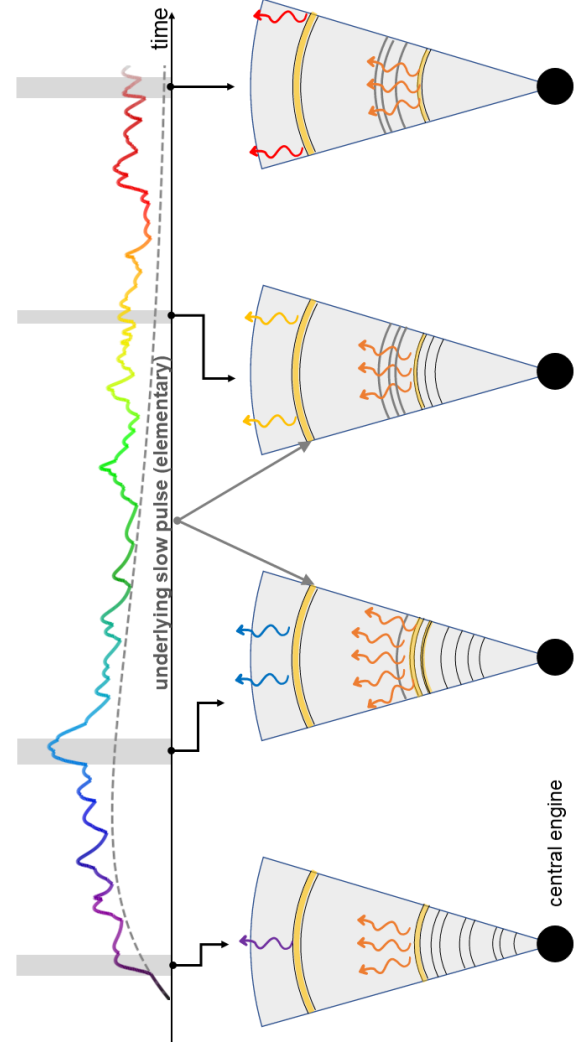


**Figure 18.** An illustration of a modified internal shock model that invokes an additional collision at a large radius from the central engine. In this case, the detected emission is a superposition of emission from fast pulses and the broad pulse. The overall light curve may indeed show shape-energy dependence, or equivalently an overall hard-to-soft trend (illustrated with colour gradient). However, the existence of an underlying slow pulse component forbids any dip features in the light curve.

to which the observed overall profile-energy dependence can be attributed.

The above mentioned features indicate that the prompt emission of this burst is from many individual emitting units that are casually linked in a emission site at a large distance from the central engine. We elaborated and demonstrated with simulations that, this scenario is consistent with the picture of many mini-jets due to local magnetic reconnection events in a large emission zone far from the GRB central engine (as envisaged in

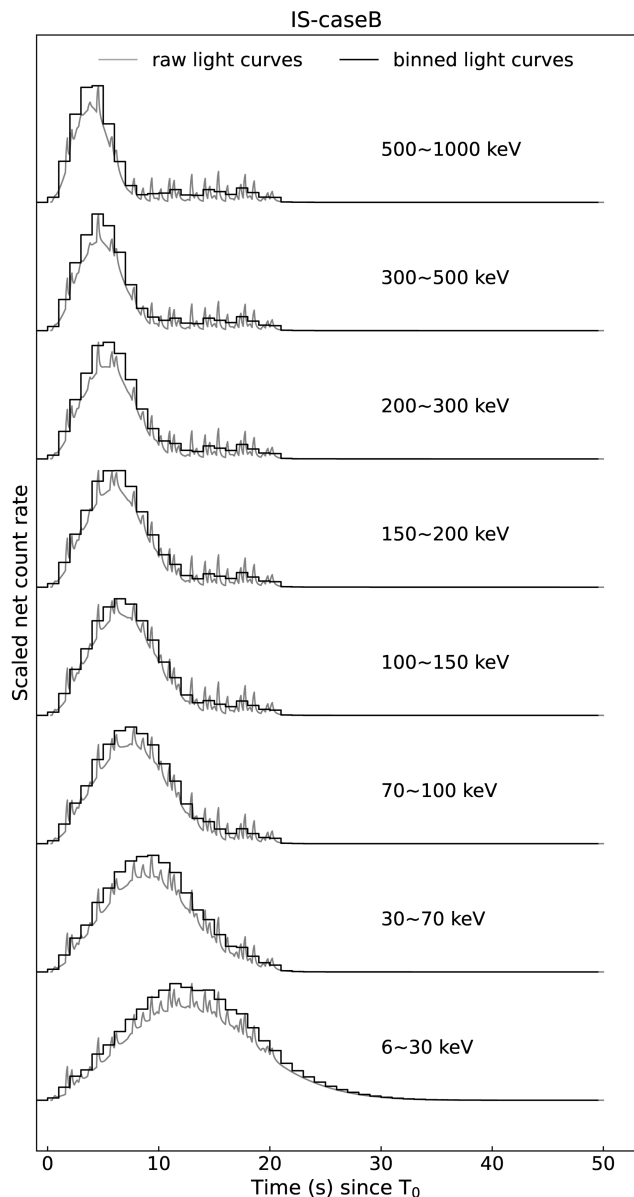


**Figure 19.** The simulated multi-band light curves within the framework of the modified internal shock model that invokes superposition a large-radius internal shock and many small-radii internal shocks. The overall light curve is dominated by the emission from the large-radius internal shock, with no hope to produce dips in the energy-dependent light curves.

the ICMART model) but raises a great challenge to the internal shock-like models that attribute all variability components to collisions among different shells.

## REFERENCES

- Bom, C. R., Kilpatrick, C. D., Santucci, R., et al. 2023, GRB Coordinates Network, 33459, 1
- Bošnjak, Ž., & Daigne, F. 2014, *A&A*, 568, A45, doi: [10.1051/0004-6361/201322341](https://doi.org/10.1051/0004-6361/201322341)
- Daigne, F., & Mochkovitch, R. 1998a, *MNRAS*, 296, 275, doi: [10.1046/j.1365-8711.1998.01305.x](https://doi.org/10.1046/j.1365-8711.1998.01305.x)
- . 1998b, *MNRAS*, 296, 275, doi: [10.1046/j.1365-8711.1998.01305.x](https://doi.org/10.1046/j.1365-8711.1998.01305.x)
- . 2003, *MNRAS*, 342, 587, doi: [10.1046/j.1365-8711.2003.06575.x](https://doi.org/10.1046/j.1365-8711.2003.06575.x)
- Drenkhahn, G., & Spruit, H. C. 2002, *A&A*, 391, 1141, doi: [10.1051/0004-6361:20020839](https://doi.org/10.1051/0004-6361:20020839)

- Fermi GBM Team. 2023, GRB Coordinates Network, 33405, 1
- Giannios, D. 2006, *A&A*, 457, 763, doi: [10.1051/0004-6361:20065000](https://doi.org/10.1051/0004-6361:20065000)
- Gillanders, J. H., Troja, E., Fryer, C. L., et al. 2023, arXiv e-prints, arXiv:2308.00633, doi: [10.48550/arXiv.2308.00633](https://doi.org/10.48550/arXiv.2308.00633)
- Goodman, J. 1986, *ApJL*, 308, L47, doi: [10.1086/184741](https://doi.org/10.1086/184741)
- Guo, S., Li, G., Zheng, J., et al. 2023, *IEEE Access*, 11, 6623, doi: [10.1109/ACCESS.2023.3236670](https://doi.org/10.1109/ACCESS.2023.3236670)
- Hakkila, J., Giblin, T. W., Norris, J. P., Fragile, P. C., & Bonnell, J. T. 2008, *ApJL*, 677, L81, doi: [10.1086/588094](https://doi.org/10.1086/588094)
- Huang, Y., Shi, D., Zhang, X., et al. 2023, arXiv e-prints, arXiv:2307.04999, doi: [10.48550/arXiv.2307.04999](https://doi.org/10.48550/arXiv.2307.04999)
- Kobayashi, S., Piran, T., & Sari, R. 1997, *ApJ*, 490, 92, doi: [10.1086/512791](https://doi.org/10.1086/512791)
- Levan, A., Gompertz, B. P., Salafia, O. S., et al. 2023a, arXiv e-prints, arXiv:2307.02098, doi: [10.48550/arXiv.2307.02098](https://doi.org/10.48550/arXiv.2307.02098)
- Levan, A. J., Gompertz, B. P., Malesani, D. B., et al. 2023b, GRB Coordinates Network, 33569, 1
- Li, X. Q., Wen, X. Y., An, Z. H., et al. 2021, *Radiation Detection Technology and Methods*, 6, 12, doi: [10.1007/s41605-021-00288-z](https://doi.org/10.1007/s41605-021-00288-z)
- Liang, E.-W., Zhang, B.-B., Stamatikos, M., et al. 2006, *ApJL*, 653, L81, doi: [10.1086/510516](https://doi.org/10.1086/510516)
- Liu, Y., Ke, G., Li, X., et al. 2021, *Radiation Detection Technology and Methods*, 6, 70, doi: [10.1007/s41605-021-00311-3](https://doi.org/10.1007/s41605-021-00311-3)
- Lyutikov, M., & Blandford, R. 2003, arXiv e-prints, astro, doi: [10.48550/arXiv.astro-ph/0312347](https://doi.org/10.48550/arXiv.astro-ph/0312347)
- Maxham, A., & Zhang, B. 2009, *ApJ*, 707, 1623, doi: [10.1088/0004-637X/707/2/1623](https://doi.org/10.1088/0004-637X/707/2/1623)
- Mészáros, P., & Rees, M. J. 2000, *ApJ*, 530, 292, doi: [10.1086/308371](https://doi.org/10.1086/308371)
- Moradi, R., Wang, C. W., Zhang, B., et al. 2024, arXiv e-prints, arXiv:2410.17189, doi: [10.48550/arXiv.2410.17189](https://doi.org/10.48550/arXiv.2410.17189)
- Narayan, R., & Kumar, P. 2009, *MNRAS*, 394, L117, doi: [10.1111/j.1745-3933.2009.00624.x](https://doi.org/10.1111/j.1745-3933.2009.00624.x)
- Norris, J. P., Bonnell, J. T., Kazanas, D., et al. 2005, *ApJ*, 627, 324, doi: [10.1086/430294](https://doi.org/10.1086/430294)
- Paczynski, B. 1986, *ApJL*, 308, L43, doi: [10.1086/184740](https://doi.org/10.1086/184740)
- Peng, Z. Y., Zhao, X. H., Yin, Y., Bao, Y. Y., & Ma, L. 2012, *ApJ*, 752, 132, doi: [10.1088/0004-637X/752/2/132](https://doi.org/10.1088/0004-637X/752/2/132)
- Rees, M. J., & Meszaros, P. 1994, *ApJL*, 430, L93, doi: [10.1086/187446](https://doi.org/10.1086/187446)
- Rees, M. J., & Mészáros, P. 2005a, *ApJ*, 628, 847, doi: [10.1086/430818](https://doi.org/10.1086/430818)
- . 2005b, *ApJ*, 628, 847, doi: [10.1086/430818](https://doi.org/10.1086/430818)
- Shao, X., & Gao, H. 2022, *ApJ*, 927, 173, doi: [10.3847/1538-4357/ac46a8](https://doi.org/10.3847/1538-4357/ac46a8)
- Sun, H., Wang, C.-W., Yang, J., et al. 2024, *National Science Review*, nwae401, doi: [10.1093/nsr/nwae401](https://doi.org/10.1093/nsr/nwae401)
- Thompson, C., Mészáros, P., & Rees, M. J. 2007, *ApJ*, 666, 1012, doi: [10.1086/518551](https://doi.org/10.1086/518551)
- Uhm, Z. L., & Zhang, B. 2014, *Nature Physics*, 10, 351, doi: [10.1038/nphys2932](https://doi.org/10.1038/nphys2932)
- . 2016, *ApJ*, 825, 97, doi: [10.3847/0004-637X/825/2/97](https://doi.org/10.3847/0004-637X/825/2/97)
- Uhm, Z. L., Zhang, B., & Racusin, J. 2018, *ApJ*, 869, 100, doi: [10.3847/1538-4357/aaeb30](https://doi.org/10.3847/1538-4357/aaeb30)
- Xiao, H., & Krucker, S. 2023, GRB Coordinates Network, 33410, 1
- Xiao, S., Liu, Y. Q., Peng, W. X., et al. 2022, *MNRAS*, 511, 964, doi: [10.1093/mnras/stac085](https://doi.org/10.1093/mnras/stac085)
- Xiong, S., Wang, C., Huang, Y., & Gecam Team. 2023, GRB Coordinates Network, 33406, 1
- Yang, Y., Troja, E., & O'Connor, B. e. a. 2024, *Nature*, 626, 742, doi: [10.1038/s41586-023-06979-5](https://doi.org/10.1038/s41586-023-06979-5)
- Yi, S.-X., Seyit Yorgancioglu, E., Xiong, S. L., & Zhang, S. N. 2024, arXiv e-prints, arXiv:2411.16174, doi: [10.48550/arXiv.2411.16174](https://doi.org/10.48550/arXiv.2411.16174)
- Zhang, B. 2018, *The Physics of Gamma-Ray Bursts*, doi: [10.1017/9781139226530](https://doi.org/10.1017/9781139226530)
- Zhang, B., & Yan, H. 2011, *ApJ*, 726, 90, doi: [10.1088/0004-637X/726/2/90](https://doi.org/10.1088/0004-637X/726/2/90)
- Zhang, B., & Zhang, B. 2014, *ApJ*, 782, 92, doi: [10.1088/0004-637X/782/2/92](https://doi.org/10.1088/0004-637X/782/2/92)
- Zhang, D., Zheng, C., Liu, J., et al. 2023, *Nuclear Instruments and Methods in Physics Research A*, 1056, 168586, doi: [10.1016/j.nima.2023.168586](https://doi.org/10.1016/j.nima.2023.168586)
- Zhao, X.-Y., Xiong, S.-L., Wen, X.-Y., et al. 2021, arXiv e-prints, arXiv:2112.05101, doi: [10.48550/arXiv.2112.05101](https://doi.org/10.48550/arXiv.2112.05101)

## 6. ACKNOWLEDGEMENT

S.-X.Y. thanks the insightful discussion with Prof. Kinwah Wu on the origin of the self-similarity of the multi-wavelength light curves of the burst. S.-X.Y. also discussed with Dr. X. L. Wang and Dr. X. Y. Song on the potential physical implication of these interesting behaviour in data. This work is supported by the National Key R&D Program of China (2021YFA0718500). S.-X.Y. acknowledges support from the Chinese Academy of Sciences (grant Nos. E329A3M1 and E3545KU2). S.-L.X. acknowledges the support by the National Natural Science Foundation of China (Grant No. 12273042). The GECAM (Huairou-1) mission is supported by the Strategic Priority Research Program on Space Science (Grant No. XDA15360000) of Chinese Academy of Sciences.